Induction Heating of Two Magnetically Independent Loads With a Single Transmitter

Emilio Plumed, *Member, IEEE*, Ignacio Lope, *Member, IEEE*, Jesús Acero, *Senior Member, IEEE*, and José Miguel Burdío, *Senior Member, IEEE*

***Abstract*—This article introduces the design of a system capable of heating two magnetically independent ferromagnetic loads placed on different horizontal planes, which uses a combination of induction heating and inductive coupling, called inductively coupled heating. The system uses a single primary inductor acting as a transmitter to transfer power to a secondary inductor attached to the bottom load, which is connected electrically with a third inductor that heats the top load. Since power of the whole system is supplied by a simple half-bridge inverter, the ratio of the delivered power to each of the loads, which is critical for cooking results, is entirely dependent on the system's geometry, coil's number of turns, and compensation capacitors. A finite-element model is used to simulate the magnetic fields generated by inductor currents and calculate the impedance matrix. With the impedance, capacitor values and inductors' number of turns are selected with the objective of achieving a high power ratio between the top and bottom zones, as well as minimizing stress in the electronics. First, a prototype was built to validate the impedance results in the small-signal regime, and then, the full power regime was used to verify power and current simulations.**

***Index Terms*—Electromagnetic analysis, finite-element method, home appliances, induction heating (IH), inductive coupling.**

I. Introduction

INDUCTION heating (IH) applied in a household environment is an advanced technological solution, actively researched on for more than 35 years [2]–[5]. The successive developments have made IH cooktops efficient [6]–[9], safe [10], fast, and easy to use and clean [11], as well as more flexible regarding the material of cooking vessels [12] and their size and number [13]–[19] . These features have turned induction cooktops into a widely accepted industrial product.

Manuscript received June 1, 2021; revised August 26, 2021; accepted September 28, 2021. Date of publication October 1, 2021; date of current version November 30, 2021. This work was supported in part by the Spanish Ministry of Science and Innovation and the Spanish State Research Agency under Project PID2019-103939RB-I00, co-funded by the European Union through the European Regional Development Fund, in part by the BSH Home Appliances Group, and in part by the Gobierno de Aragón-FSE 2014-20 under Grant IIU/2023/2017. This article is an extension of a conference paper [1]. Recommended for publication by Associate Editor M. Vitelli. *(Corresponding author: Emilio Plumed.)*

Emilio Plumed, Jesús Acero, and José Miguel Burdío are with the Department of Electronic Engineering and Communications, Universidad de Zaragoza, 50009 Zaragoza, Spain (e-mail: eplumed@unizar.es; jacero@unizar.es; burdio@unizar.es).

Ignacio Lope is with BSH Electrodomésticos España, 50197 Zaragoza, Spain, and also with the Department of Applied Physics, Universidad de Zaragoza, 50009 Zaragoza, Spain (e-mail: nlope@unizar.es).

Color versions of one or more figures in this article are available at https://doi.org/10.1109/TPEL.2021.3117146.

Digital Object Identifier 10.1109/TPEL.2021.3117146

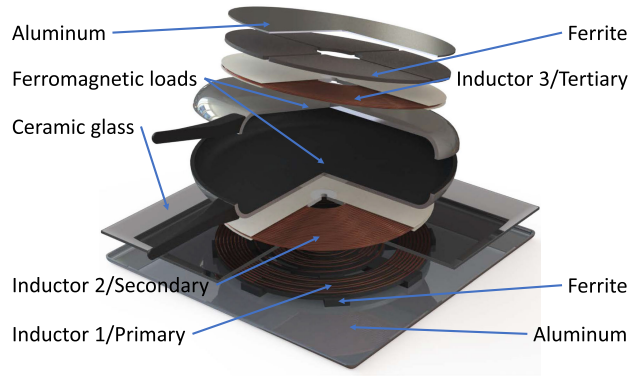

Fig. 1. Exploded system geometry.

In these cooktops, energy is transferred through electromagnetic induction directly from its inductors to the vessel without needing physical contact among its components [20], [21]. In a similar manner, wireless power transfer (WPT) systems also use electromagnetic induction to transfer energy from a transmitting coil to a receiving coil [22]–[24], with continuous advances in topologies and control [25]–[27] and coil design [28].

Typical WPT applications use additional power electronics in their receiver side, such as rectifiers and dc–dc stages, to better control output voltage and power and make them immune to load variation and system misalignment. Currently, there is an increasing demand for small appliances that use WPT technology, and many of them require heating. Moreover, IH cooktops already have planar inductors that can wirelessly transmit power to other planar inductors. Additionally, some of these appliances require heating areas independent from its bottom surface, unreachable by IH alone or other conventional cooking technologies, such as gas or electric glass ceramic.

Hybrid systems can transfer energy from inductor to inductor while simultaneously heating ferromagnetic loads. Since IH and WPT can operate at the same frequencies, rectification and further inversion are redundant, and the additional electronics in the receiver side can be removed.

This kind of hybrid system can be used to create cordless portable ovens and double-sided pans, where both upper and lower baking sheets are heated simultaneously, as shown in Figs. 1 and 2. The main advantages of this kind of cooking appliance are their enclosed space to prevent heat loss, such as an oven, and their small volume to reduce energy requirements. A wide array of foods and dishes can benefit from the heating on both sides. Instead of flipping manually to keep both sides

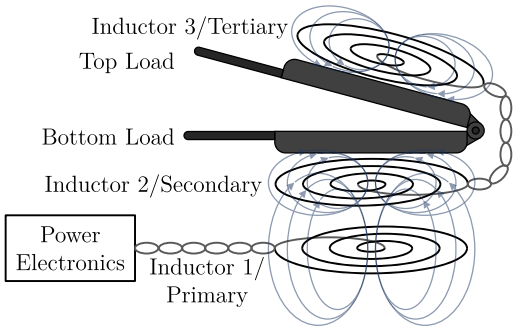

Fig. 2. Inductor connection diagram.

heated, the proposed system will heat both sides simultaneously, with a single correct "upright" position.

This capability cannot be provided by the high-range flexible IH appliances based on a matrix of small inductors [13], [15], [17], [19]. Moreover, in high-range appliances, each coil is energized by an inverter, with the subsequent increase in cost and complexity. However, the proposed system only requires one inverter to feed two loads without additional internal power sources or external cables.

Inductively coupled heating (ICH), defined as the combination of IH and magnetic coupling, has been used to improve working conditions for previously inefficient situations in conventional IH [29]–[31] and also to give new inductively coupled functionality [1], [32]–[34]. Other works offer both IH and wireless magnetic coupling functionality independent of one another [35]. In this case, a system with an additional magnetically independent cooking zone is proposed, where only a single inductor is fed externally to heat a coupled bottom load and transmit power to a secondary inductor, which, in turn, is electrically connected to a third coil to heat an independent top load. Essentially, a single primary cooktop inductor is able to deliver power to two different loads simultaneously, which can be placed in different planes, preventing their coupling. In the case of Fig. 1, the uncoupled heating zone is the top cover of a small slim oven. In its current form, the first and second inductors need to be aligned, and the bottom cooking zone is placed just above the secondary inductor. Nevertheless, the third inductor and top cooking zone or vessel can be placed anywhere, requiring only an electric connection to the secondary coil, as depicted in the diagram in Fig. 2.

The objective of this article, as an extension of the work presented in [1], is to design and test a 210-mm ∅ ICH system capable of delivering 3000 W to two ferromagnetic loads, where at least 50% of the power is transferred to the uncoupled top load. This requirement ensures that the system can give more heat to the top load in order to cook meals that need higher temperature on the top and to correct imbalances in processes that require homogeneous temperature. The position of the loads prevents coupling between their corresponding inductors and, thus, requires an electrical connection. The system must also work in conjunction with a conventional IH cooktop to reduce cost. As a result, instead of using state-of-the-art resonant converters [5], a humble half-bridge inverter is used to feed the primary inductor. The half-bridge inverter is one of the most popular topologies due to its small number of devices, compact size, small conduction and switching losses, ease of control, low electromagnetic interference, and capabilities of multifrequency operation and ac–ac power conversion. Moreover, with this solution, the secondary inductor does not need a cord to connect to the mains, an inverter topology of its own or bulky filters.

The power flow in the system goes as follows: the IH cooktop feeds the primary inductor, which simultaneously heats the bottom load and transfers power to the second inductor. The second inductor contributes to heating the bottom load and is electrically connected to the third inductor. The sole purpose of the third inductor is to heat the top load.

The main contribution of this article is the transfer of more than half the total power to the top load using only one energized inductor with impedance tuning and no additional active components, despite the fact that the bottom load and the top load are electromagnetically uncoupled. No current commercial IH appliance can transmit power simultaneously to both halves of a double-sided pan. Although there are works that use the same technology, to the best of our knowledge, no similar enough systems have been proposed in the literature.

The rest of this article is organized as follows. Section II introduces the system's circuit model and its most relevant parameters. The system's simulation and finite-element analysis (FEA) tool are explained in Section III. Section IV introduces the experimental verification and simulation validation. Finally, Section V concludes this article.

II. System Model

The modeled system depicted in Fig. 1 consists of a 210-mm ∅ primary inductor with ferrite bars and an aluminum tray, a 210-mm ∅ secondary inductor attached to the bottom ferromagnetic load, and a third inductor of the same size attached to the top ferromagnetic load. The first and second inductors are separated by ceramic glass, and the third inductor has a ferrite plane and a second aluminum tray above it for magnetic shielding.

The circuit diagram of a generic three-inductor system is shown in Fig. 3(a). Throughout most of this article, the calculations use phasors in the frequency domain, assuming that only the first-order harmonic is relevant. This circuit can be expressed in the form of a matrix equation [15]

$$\begin{pmatrix} Z_{11} & Z_{12} & Z_{13} \\ Z_{21} & Z_{22} & Z_{23} \\ Z_{31} & Z_{32} & Z_{33} \end{pmatrix} \begin{pmatrix} I_1 \\ I_2 \\ I_3 \end{pmatrix} = \begin{pmatrix} V_1 \\ V_2 \\ V_3 \end{pmatrix} \tag{1}$$

where I_i is the current of the ith inductor, V_i is its external voltage, and Z_{ij} are the elements of the impedance matrix, where Z_{ii} is the sum of the self-impedance of the ith inductor, $Z_{\text{ind},ii}$, plus that of the compensation capacitor, C_i, if present, and Z_{ij} is the mutual impedance between inductors

$$Z_{ii} = Z_{\text{ind},ii} + 1/j\omega C_i = R_{ii} + j\omega L_{ii} + 1/j\omega C_i \tag{2}$$

$$Z_{ij} = Z_{\text{ind},ij} = R_{ij} + j\omega L_{ij},\ i \neq j \tag{3}$$

where the involved terms are shown in Fig. 3(a). Coupling factors can be defined for mutual inductance and resistance, $k_{l,ij}$ and $k_{r,ij}$, respectively

$$k_{l,ij} = L_{ij}/\sqrt{L_{ii}L_{jj}} \tag{4}$$

$$k_{r,ij} = R_{ij}/\sqrt{R_{ii}R_{jj}}. \tag{5}$$

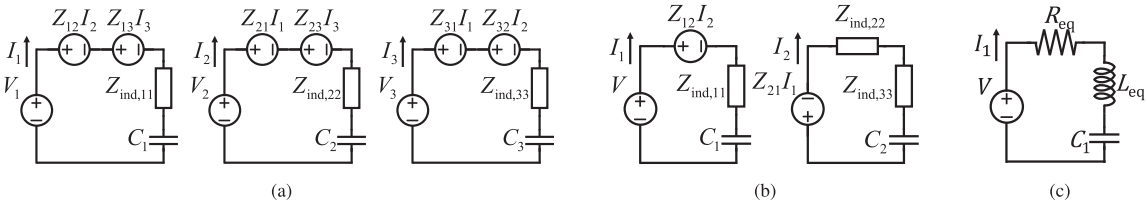

Fig. 3. Circuit diagrams. (a) Generic three inductors. (b) Proposed system's simplified circuit. (c) Inverter equivalent impedance circuit.

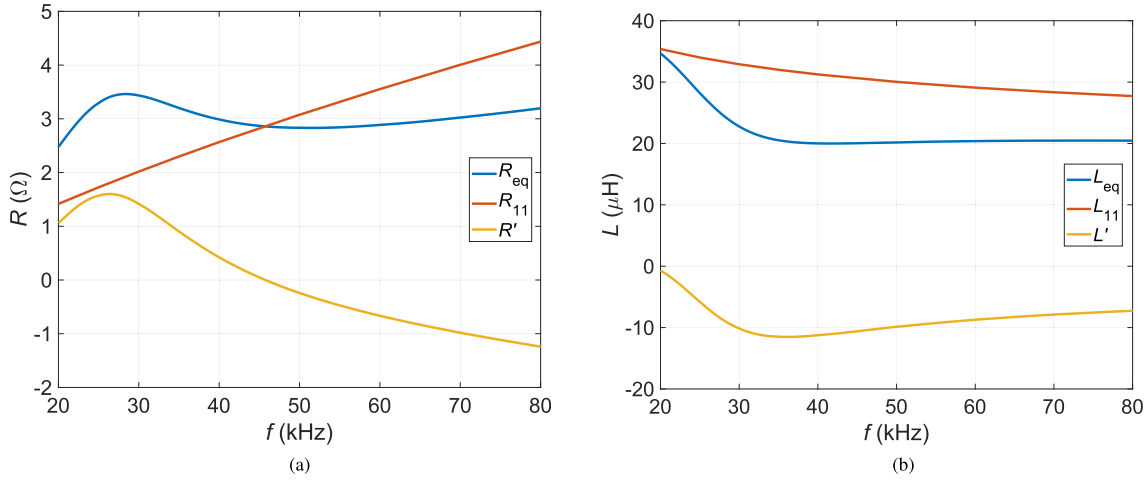

Fig. 4. Equivalent (a) resistance and (b) inductance breakdown according to (12) and (13).

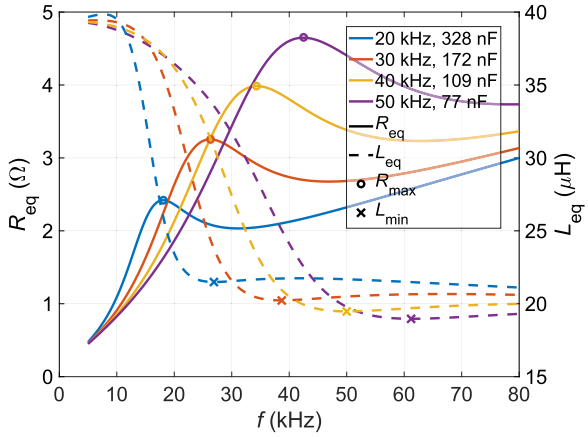

Fig. 5. Simulated equivalent resistance and inductance versus frequency for different $\omega_{0,\mathrm{rec}}$, with specific C_2 values.

In this case, the second and third inductors are connected in series. Therefore, only two resonant capacitors are needed, one for the primary inductor and the other for the receiver side, i.e., the series-connected second and third inductors. The equations can, then, be simplified, as the current running through both inductors is the same and the voltage sum is zero since there is no external feed

$$I_2 = I_3 \tag{6}$$

$$V_2 + V_3 = 0. \tag{7}$$

Therefore, the reduced-order equation system is

$$\begin{pmatrix} Z_{11} & Z_{12}+Z_{13} \\ Z_{21}+Z_{31} & Z_{22}+2Z_{23}+Z_{33} \end{pmatrix} \begin{pmatrix} I_1 \\ I_2 \end{pmatrix} = \begin{pmatrix} V_1 \\ 0 \end{pmatrix}. \tag{8}$$

In this system, the third inductor will heat a load inaccessible to the first two, as both loads are magnetically independent. Consequently, the terms Z_{13} and Z_{23} are considered negligible, which will also be verified in the simulations. The equations can, then, be simplified to

$$\begin{pmatrix} Z_{11} & Z_{12} \\ Z_{21} & Z_{22}+Z_{33} \end{pmatrix} \begin{pmatrix} I_1 \\ I_2 \end{pmatrix} = \begin{pmatrix} V_1 \\ 0 \end{pmatrix} \tag{9}$$

and the resulting simplified circuit is shown in Fig. 3(b). Moreover, the magnetic independence of the top load and the third inductor makes Z_{33} the only impedance matrix element related to the top load. Z_{11}, Z_{12}, and Z_{22} all relate to the bottom load.

The primary inductor is fed by a half-bridge inverter [11], as it is typical in conventional IH cooktops, forming the LC series resonant tank by connecting the primary inductor to its capacitor. Therefore, a global equivalent impedance [30], $Z_{\mathrm{eq}} = V_1/I_1$, can be defined from the inverter's point of view

$$Z_{\mathrm{eq}} = Z_{11} - \frac{Z_{12}^2}{Z_{22}+Z_{33}} \tag{10}$$

$$Z_{\mathrm{eq}} = R_{\mathrm{eq}} + j(\omega L_{\mathrm{eq}} - 1/\omega C_1) \tag{11}$$

where R_{eq} is the equivalent resistance and L_{eq} is the equivalent inductance. The resulting equivalent circuit is shown in Fig. 3(c). Developing (10) and (11), the full expressions of R_{eq} and L_{eq}

are

$$R_{\text{eq}} = R_{11} + \underbrace{\frac{2R_{12}\omega L_{12}\left(\omega L_{\text{rec}} - \frac{1}{\omega C_2}\right) - \left(R_{12}^2 - \omega^2 L_{12}^2\right) R_{\text{rec}}}{R_{\text{rec}}^2 + \left(\omega L_{\text{rec}} - \frac{1}{\omega C_2}\right)^2}}_{R'} \tag{12}$$

$$L_{\text{eq}} = L_{11} + \underbrace{\frac{2R_{12}\omega L_{12}R_{\text{rec}} - \left(R_{12}^2 - \omega^2 L_{12}^2\right)\left(\omega L_{\text{rec}} - \frac{1}{\omega C_2}\right)}{\omega\left(R_{\text{rec}}^2 + \left(\omega L_{\text{rec}} - \frac{1}{\omega C_2}\right)^2\right)}}_{L'} \tag{13}$$

where $R_{\text{rec}} = R_{22} + R_{33}$, $L_{\text{rec}} = L_{22} + L_{33}$, and R' and L' are the resistance and inductance reflected to the primary side, respectively. For visual reference, the contributions of the elements R_{11}, R' and L_{11}, L' to R_{eq} and L_{eq}, respectively, are represented in Fig. 4. R' increases R_{eq} at the low frequency range, with a maximum peak, and decreases it in others. L' only decreases L_{eq} at the considered frequency range, with a minimum valley close to the R_{eq} peak. These impedance peaks and valleys are the cause of the phenomenon known in WPT applications as pole splitting or bifurcation, which can cause an additional peak to appear in the power curve or generate several zero-crossing points of the angle of equivalent impedance. Pole splitting can disrupt the monotonic relation between frequency and power for the ICH system, which makes minimizing its effects a priority. The easiest solution is to separate the impedance extreme values from the resonant frequency of the system's equivalent impedance, $\omega_{0,\text{eq}}$, which can be determined from (11)

$$\omega_{0,\text{eq}} = 1/\sqrt{L_{\text{eq}}C_1}. \tag{14}$$

Similarly, the receiver side composed of the second and third inductors with the second compensation capacitor has its own resonant frequency, $\omega_{0,\text{rec}}$, defined as [30], [34]

$$\omega_{0,\text{rec}} = 1/\sqrt{(L_{22} + L_{33})C_2} \tag{15}$$

which is very relevant for the equivalent impedance and other parameters, as C_2 appears in the expressions for both R_{eq} (12) and L_{eq} (13), making it responsible for the R' peak and L' valley. Fig. 5 shows simulated impedance values for the proposed system, changing C_2 and keeping the values of the number of turns and C_1 constant. The values of C_2 are determined using (15) to achieve the stated $\omega_{0,\text{rec}}$ for each color. As shown, the impedance can be in the same order of magnitude as the values of a typical domestic IH application [8]. Moreover, both R_{eq} and L_{eq} are strongly dependent on frequency, with maximum and minimum values marked with circles and crosses, respectively. Maximum R_{eq} values are found slightly to the left of $\omega_{0,\text{rec}}$, while minimum L_{eq} values are found slightly to the right.

These extreme values of impedance close together in frequency also affect other derived values, such as the power ratio, PR_{top}, between the top ferromagnetic load power, $P_{\text{load,top}}$, and the total transferred power, P_{total}, defined as $\text{PR}_{\text{top}} = P_{\text{load,top}}/P_{\text{total}}$. Top power ratio, PR_t, is simply an indicator of the power split between the top and bottom loads and should not be confused with efficiency, defined as $\eta = P_{\text{losses}}/P_{\text{total}}$. Expressions for the losses' elements can be found in [8] and[14].

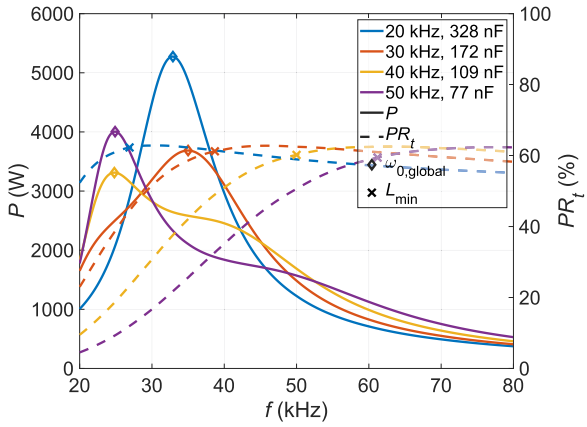

Fig. 6. Simulated total power and percentage of power delivered to the top load versus frequency for different $\omega_{0,\text{rec}}$.

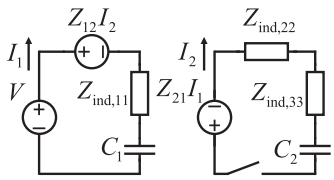

Fig. 7. Circuit diagram with a switch on the receiver side.

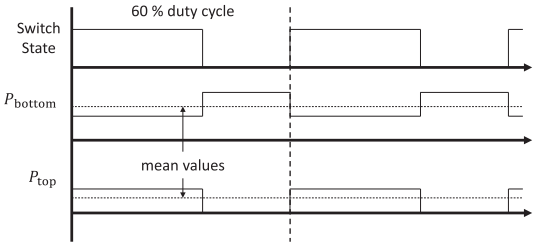

Fig. 8. Power split diagram depending on the receiver connection state.

PR_t can be expressed in terms of current ratios and impedances as

$$\text{PR}_{\text{top}} = \frac{P_{\text{load,top}}}{P_{\text{total}}} = \frac{R_{33}|I_3|^2}{R_{\text{eq}}|I_1|^2} = \frac{R_{33}|Z_{21}|^2}{R_{\text{eq}}|Z_{22} + Z_{33}|^2} \tag{16}$$

considering that $P_{\text{total}} = P_{\text{load,bottom}} + P_{\text{load,top}}$, where $P_{\text{load,bottom}}$ is the power delivered to the bottom load. PR_{top} has a maximum value at frequencies close to the inductance minimums, as shown in Fig. 6, for the same parameters of Fig. 5. The shift of $\omega_{0,\text{rec}}$ causes a change in L_{eq}, as explained previously, which, in turn, causes a change in $\omega_{0,\text{eq}}$ from 35 to 25 kHz.

In Fig. 6, it can also be seen that for most of the power curve, the ratio of the power delivered to the top load is almost constant at 60%, so this design is most suitable for applications, where the power ratio needs to remain nearly constant for all delivered power values.

A degree of independent power control can be achieved using a switch on the receiver side to open the circuit, as depicted in Fig. 7. The switch would enable alternating the power split between 100% and 0%, and 40% and 60%. Time averages can be used to interpolate intermediate ratios, as depicted in Fig. 8. Higher PR_{top} would enable a wider range of power splits.

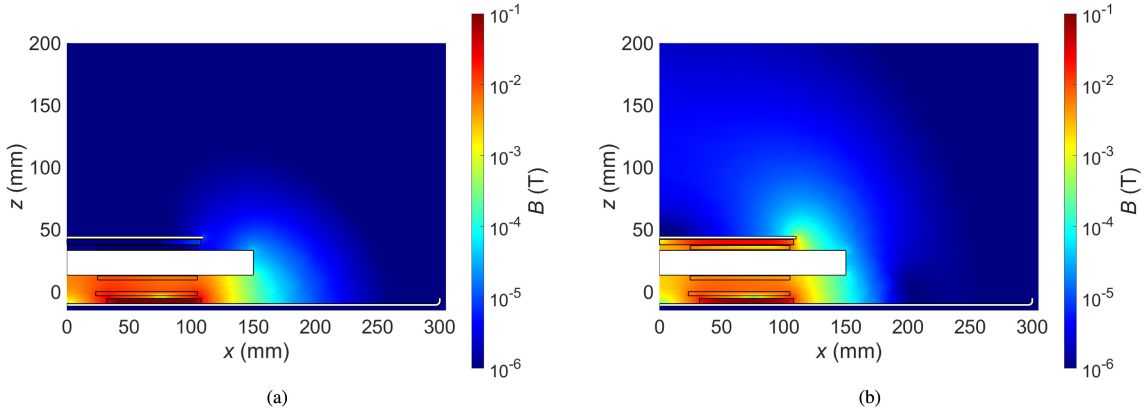

Fig. 9. Simulated magnetic field to deliver 3000 W. (a) First inductor only. (b) Full ICH system.

TABLE I
RESISTANCE VALUES OF THE IMPEDANCE MATRIX AT 30 KHZ

i \ j	$R_{i1,\text{s.t.}}(\text{m}\Omega)$	$R_{i2,\text{s.t.}}(\text{m}\Omega)$	$R_{i3,\text{s.t.}}(\text{m}\Omega)$
$R_{1j,\text{s.t.}}$	6.72	8.59	0.00202
$R_{2j,\text{s.t.}}$	8.59	11.1	0.00187
$R_{3j,\text{s.t.}}$	0.00202	0.00187	18.8

TABLE II
INDUCTANCE VALUES OF THE IMPEDANCE MATRIX AT 30 KHZ

i \ j	$L_{i1,\text{s.t.}}(\text{nH})$	$L_{i2,\text{s.t.}}(\text{nH})$	$L_{i3,\text{s.t.}}(\text{nH})$
$L_{1j,\text{s.t.}}$	114	76.2	0.00671
$L_{2j,\text{s.t.}}$	76.2	97.4	0.00891
$L_{3j,\text{s.t.}}$	0.00671	0.00891	110

III. SYSTEM SIMULATION

A. Finite-Element Analysis

In order to obtain the impedance matrix, the system was simulated in Comsol Multiphysics. The 210-mm ∅ inductors are modeled as low-loss disks with a uniform current density distributed in a single turn and the ferromagnetic loads as impedance boundary conditions [36]. The material properties for the loads are a conductivity of 2×10^7 S/m and a relative permeability of 400–175i [15]. These are characteristics of the material that will be used for testing at 100 °C. The impedance relation between single-turn and multiturn coils is [8]

$$Z_{ij} = n_i n_j Z_{ij,\text{s.t.}} \tag{17}$$

where n_i is the number of turns of the ith inductor and $Z_{ij,\text{s.t.}}$ is the single-turn impedance of element ij. For this to remain true when $i = j$, capacitor values also need to change with the number of turns

$$C_i = C_{i,\text{s.t.}}/n_i^2 \tag{18}$$

where $C_{i,\text{s.t.}}$ is a mathematical *single-turn* capacitor [30] that enables the relation

$$X_{ii} = n_i^2(\omega L_{ii,\text{s.t.}} - 1/\omega C_{i,\text{s.t.}}) = n_i^2 X_{ii,\text{s.t.}} \tag{19}$$

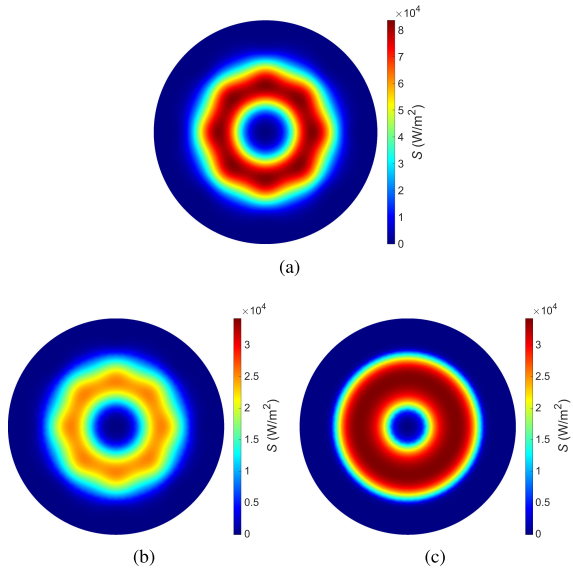

Fig. 10. Simulated power density to deliver 3000 W. (a) First inductor only. (b) Full ICH system bottom. (c) Full ICH system top.

where X_{ii} is the reactance of the ii matrix element and $X_{ii,\text{s.t.}}$ is the single-turn reactance.

Each element of the impedance matrix, $Z_{\text{ind},ij,\text{s.t.}}$, is obtained by driving an external current through inductor i and computing induced voltage in inductor j [13].

Impedance results at 30 kHz are given in Tables I and II for the simulated geometry of 210-mm ∅ inductors shown in Fig. 9, where the simplification made in (9) is justified. Applying (4) and (5), the coupling factors for the table values are $k_{l,12} = 0.7231$ and $k_{r,12} = 0.9946$. As expected, the symmetry in the impedance matrix, i.e., the relation $Z_{ij} = Z_{ji}$, is also verified.

Fig. 9 represents the simulated magnetic field generated, first by only the first inductor, in an IH configuration, and then by the full ICH system when delivering 3000 W. The field levels are similar in both cases, with more magnitude in the IH case in the radial direction and more magnitude in the ICH case in the vertical direction.

Fig. 10 represents the simulated electromagnetic power density, S, in the loads, first in the IH case and then by the full ICH system when delivering 3000 W.

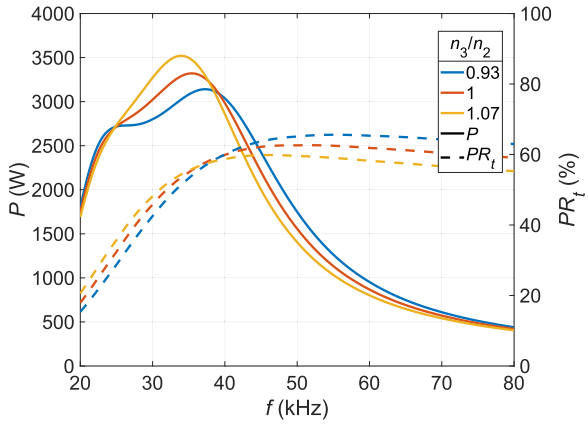

Fig. 11. Simulated power and power ratio variation with n_3/n_2.

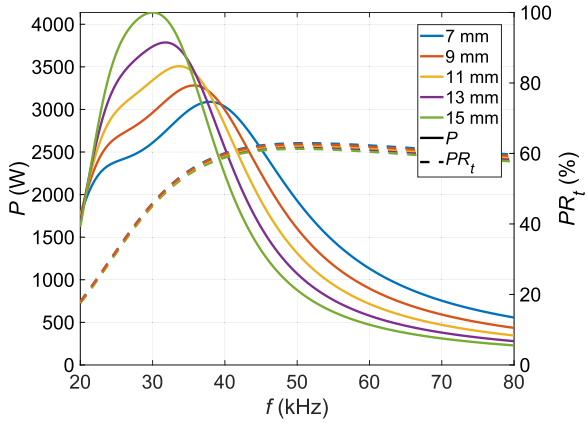

Fig. 12. Simulated power and power ratio variation with inductor distance.

TABLE III
EXPERIMENTAL SYSTEM DESIGN PARAMETERS

Inductor	n_i	C_i (nF)
1, primary	17	1080
2, secondary	29	150
3, tertiary	29	–

B. System Design

The finite-element simulation has provided the single-turn inductor elements of the impedance matrix. Now, it remains to select the number of turns of each inductor and the capacitor values. As part of a half-bridge IH appliance, the power is frequency controlled. Consequently, the ICH system needs to have a monotonic relation between frequency and power, from 0 to 3000 W.

As the system must be compatible with an existing IH cooktop, the capacitor value and the inductor number of turns on the primary side are predetermined. For this article, the values that can be changed by design are the number of turns of the second and third inductors as well as the second resonant capacitor.

In order to operate at a relatively constant PR_{top}, the working frequencies have to be greater than those of the maximum R_{eq} and minimum L_{eq}, as seen in Figs. 5 and 6. These extreme values are related to the resonance of the receiver side, $\omega_{0,\text{rec}}$.

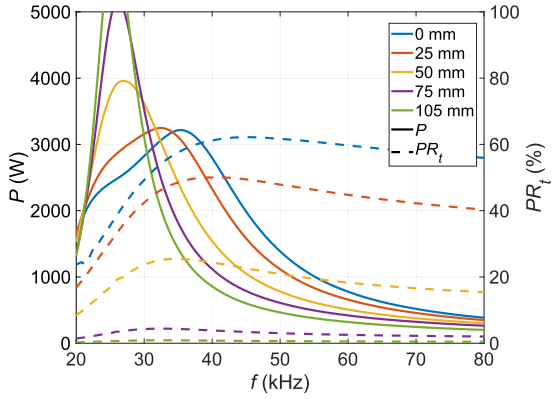

Fig. 13. P and PR_t variation with radial load misalignment.

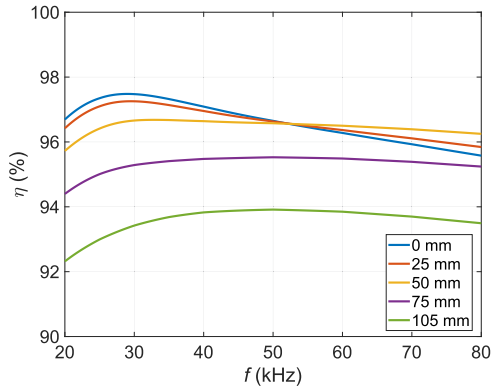

Fig. 14. Efficiency variation with load misalignment.

In most cases, the maximum power, P_{max}, is obtained at the equivalent system's resonance, $\omega_{0,\text{eq}}$. The power ratio is desired to remain constant up to P_{max}, so global resonance has to be set at a slightly higher frequency than the receiver-side resonance, which can be seen in Fig. 6. When $\omega_{0,\text{rec}}$ is set at 20 and 30 kHz, $\omega_{0,\text{eq}}$ is above 30 kHz and PR_{top} ranges between 50% and 60%. Moreover, when $\omega_{0,\text{rec}}$ is set at 40 and 50 kHz, $\omega_{0,\text{eq}}$ is below 30 kHz and PR_{top} ranges between 10% and 60%. Fig. 5 also shows that the receiver-side resonance causes an inflection point in the power curve as well as the impedance extreme values.

Combining (10) and (17), Z_{eq} can be expressed in terms of single-turn impedance matrix elements as

$$Z_{\text{eq}} = n_1^2 \left(Z_{11,\text{s.t.}} - \frac{Z_{12,\text{s.t.}}^2}{Z_{22,\text{s.t.}} + \frac{n_3^2}{n_2^2} Z_{33,\text{s.t.}}} \right). \tag{20}$$

This expression shows that the receiver-side inductors' number of turns only affect the equivalent impedance by their relative values to each other. Moreover, for each fixed value of n_3/n_2, the impedance only depends on the primary inductor's number of turns.

The design process goes as follows. In order to be able to deliver 3000 W with near constant PR_{top}, the system must have a global resonance at higher frequency than receiver resonance, and the equivalent resistance needs to satisfy $V_{o,\text{rms}}^2/R_{\text{eq}} > 3000$ W at global resonance [17], where $V_{o,\text{rms}}$ is the inverter output rms voltage. The half-bridge inverter uses a small dc-bus

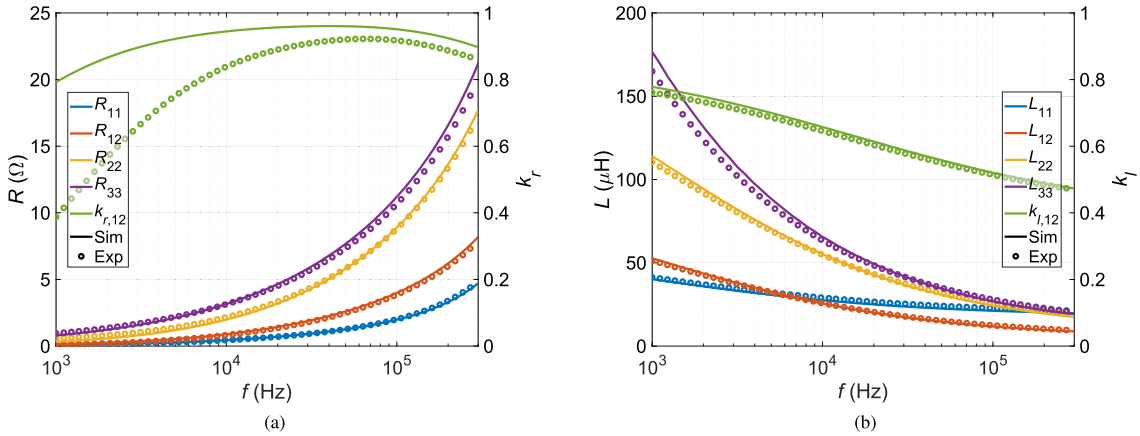

Fig. 15. (a) Resistance and (b) inductance of the impedance matrix elements measured by the LCR meter.

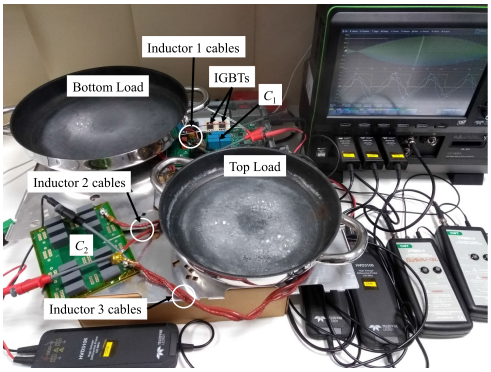

Fig. 16. Experimental setup with both bottom and top loads' boiling water.

capacitor, so its output voltage will essentially modulate the rectified mains voltage: $V_{o,\text{rms}} = \sqrt{2}/\pi V_{\text{mains,rms}}$. In terms of the number of turns and capacitor values, $C_{2,\text{s.t.}}$ can be selected to fix $\omega_{0,\text{rec}}$ at the desired value

$$C_{2,\text{s.t.}} = 1/\left(\omega_{0,\text{rec}}^2(L_{22,\text{s.t.}} + n_3^2/n_2^2 L_{33,\text{s.t.}})\right). \quad (21)$$

After selecting a potential $\omega_{0,\text{rec}}$, the designer must ensure that the 3000-W maximum power condition is met, as well as verify that $\omega_{0,\text{rec}} < \omega_{0,\text{eq}}$.

Since only the relative value of n_2 with n_3 affects global impedance, their absolute values can be used to freely select the ratio of inductor voltage and current when delivering the same power. The effects of the n_3/n_2 ratio on P and PR_{top} are shown in Fig. 11 . An increase in the ratio increases P_{max} and PR_{top} and reduces $\omega_{0,\text{eq}}$. The blue line shows a bump that is almost a second power peak caused by mild pole splitting. In this case, $n_2 = n_3$ has been chosen for simplicity, as it fulfills the PR_{top} requirement using identical coils, simplifying the manufacturing process. Additionally, if the shielding of the third inductor was not required, the equal number of turns would enable a symmetrical design without designated top or bottom loads. PR_{top} would be maintained, whichever side ended up on top.

The system is intended to work with an IH cooktop, which has a 4–5-mm thick ceramic glass. Additionally, depending on the final design, the housing of the proposed system would add an additional 4–5 mm to the distance between primary and secondary inductors. The FEA simulations have assumed a total 9-mm distance between inductors. Fig. 12 shows the effects of increasing inductor distance on P and PR_{top}. Separating the receiver increases maximum P and reduces $\omega_{0,\text{eq}}$, but it barely has an effect on PR_{top}. As a result, PR_{top} is slightly reduced at maximum power.

Usually, small adjustments need to be made in order to end up with an integer number of turns and available capacitor values. The prototype in this article has a predetermined number of turns and capacitor for the primary inductor, 17 turns and 1080 nF, the selected number of turns for the second and third inductors are 29 turns, and the selected second capacitor has 150 nF. This results in a $\omega_{0,\text{eq}}$ of 35 kHz and $\omega_{0,\text{rec}}$ of 30 kHz. The system parameters are listed in Table III for convenience.

A high number of turns were chosen for the second and third inductors to show that their absolute value would only affect the current and voltage ratio in the receiver side, and that the equivalent impedance would remain constant as long as the value of $C_{2,\text{s.t.}}$ was maintained by changing C_2 accordingly.

As any IH application, the system could be subjected to rapid movements by the user. Fig. 13 shows how P and PR_t change with radial misalignment, illustrating that for any misalignment, the system will immediately reduce its power and power ratio. Moreover, the P and PR_t changes are significant even for displacements smaller than 25 mm. The simulated efficiency does not decrease considerably with misalignment, as shown in Fig. 14, where the minimum value remains above 93%. Due to how the system works inherently, it does not need complex control to operate safely, and it is easy to detect misalignment and warn the user to correct it and maximize PR_t again.

IV. Experimental Measurements

First, in order to verify the impedance simulation results, measurements of the impedance matrix have been taken in a small-signal regime at several frequencies. Then, the system has been tested delivering full power to two ferromagnetic loads to validate the proposed design.

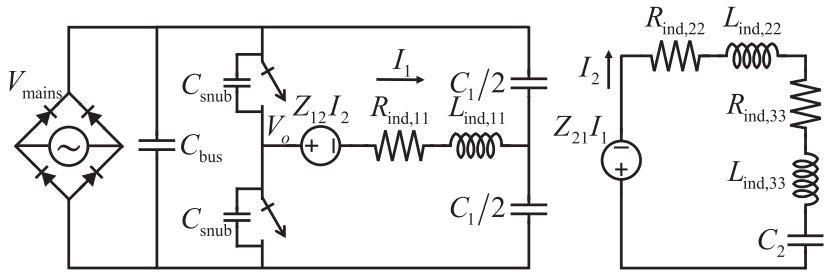

Fig. 17. Prototype's circuit diagram.

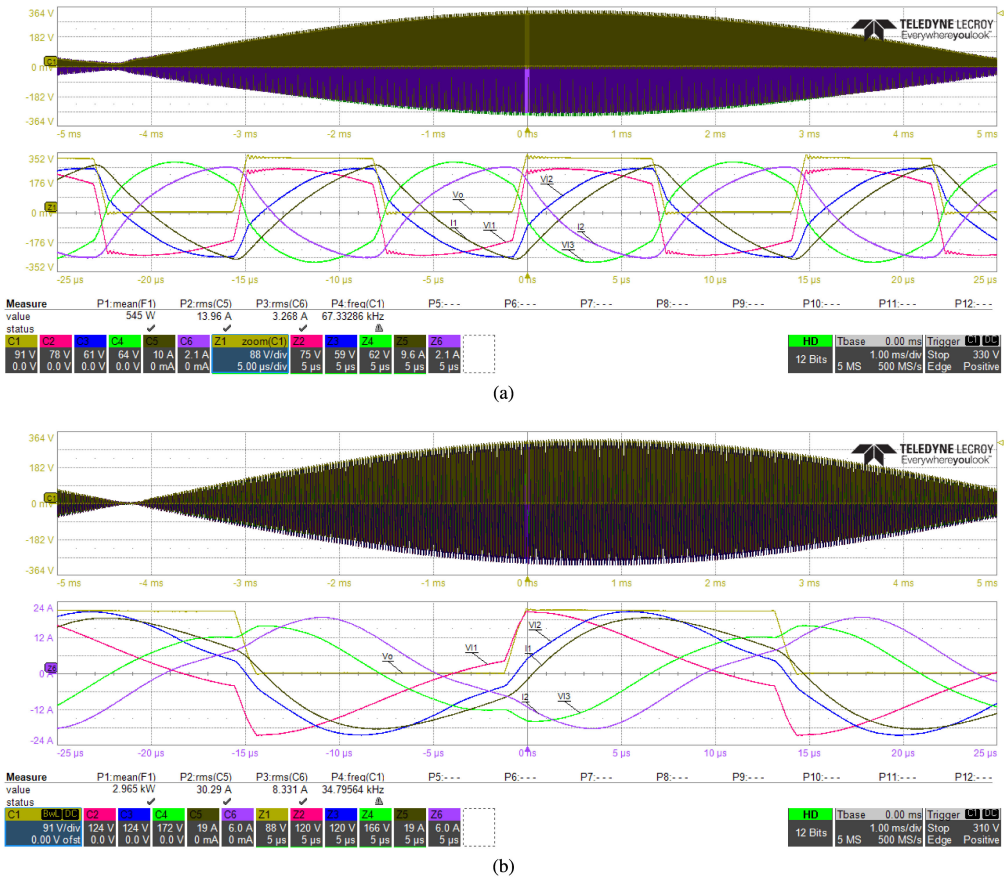

Fig. 18. Oscilloscope captures at (a) 500 W and (b) 3000 W.

A. *Small-Signal Regime*

An LCR meter has been used to measure self-impedance of first, second, and third inductors as well as the mutual impedance between the first and second inductors. Given that the third inductor is decoupled from the rest, as verified in the simulations, mutual impedances with the third inductor have not been considered.

While self-impedances were measured directly, the mutual impedance was calculated from two indirect measurements. The difference between in-phase and opposite-phase measurements of the series-connected inductors cancels out the self-impedance contribution [1].

Fig. 15 shows simulated values with continuous lines and experimental values in dots. Most impedance curves show very good agreement, with a maximum error of 7%.

(a) (b)

Fig. 19. Functional prototype. (a) Closed lid. (b) Fully open.

The coupling factors, as indirect measurements, are more divergent.

Overall, these measurements verify the simulation accuracy for the given geometry and frequencies, with material properties congruent with small-signal analysis. The results are encouraging to go ahead to the following full power test.

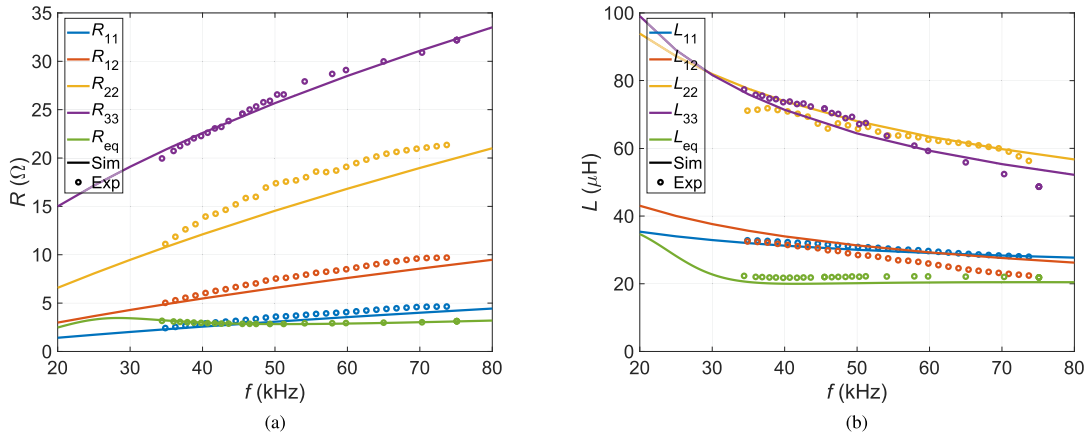

Fig. 20. Comparison between simulated and experimental impedance: (a) R and (b) L.

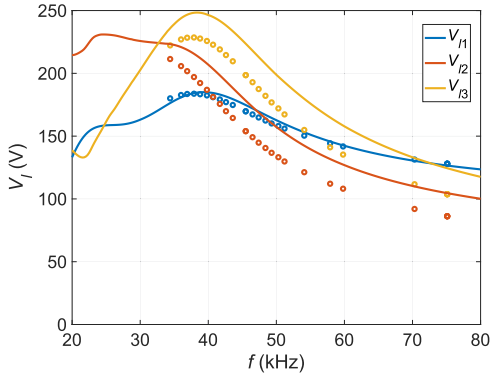

Fig. 21. Inductor voltages, both simulated and measured.

B. *Full Power Regime*

As mentioned in Section II, the system is fed by a half-bridge inverter, which modulates the rectified mains voltage [11]. The relevant parts of the simulated geometry remain the same, such as distances between inductors and loads, diameters, and so on. However, in order to help heat dissipation in the experimental measurements and maintain ferromagnetic material properties with constant temperature, the independent load is a second water-filled pan, as seen in Fig. 16, flipping the top half of the small oven. This partition of the geometry is valid as long as each half maintains their relative geometry and materials of the original, and the inductors are kept far enough away to avoid coupling.

In the experimental setup, the first inductor is connected to the IH appliance's inverter and placed beneath the "bottom" load. The second inductor is placed above the first inductor and beneath the bottom load and connected to the C_2 capacitor board and the third inductor. The third inductor is likewise connected to the second inductor and the C_2 board, and it is placed beneath the "top" load.

The circuit diagram, including inverter, inductors, and loads, is shown in Fig. 17. The main differences with Fig. 3 are the voltage input to the system and the bifurcation of C_1. The mains voltage is rectified in a full-diode bridge, it is filtered by a 3.3-μF capacitor, and it is inverted by an insulated-gate bipolar transistor (IGBT) half-bridge inverter. The transistors use 15-nF snubber capacitors to minimize turn-OFF losses. The C_1 capacitor is split to ensure zero dc voltage and eliminate all even harmonics. The inverter uses frequency control to deliver power up to 3000 W.

Waveforms have been captured with an oscilloscope of inverter output voltage V_o, primary inductor voltage V_{L1}, second inductor voltage V_{L2}, third inductor voltage V_{L3}, primary inductor current I_1, and secondary inductor current I_2. Sample captures when delivering 500 and 3000 W are shown in Fig. 18. At low power, in Fig. 18(a), the waveforms have almost triangular and exponential shapes, while at high power, in Fig. 18(b), the waveforms are more sinusoidal.

In addition to the experimental setup to take measurements, a functional prototype has also been built and shown in Fig. 19. The compartmentalization of the electronics and their position near the hinge, away from the loads, are enough to prevent the high temperatures from reaching the ceramic capacitors.

Calculations up to now have assumed the first-order harmonic for its frequency calculations. In order to better determine the accuracy of the FEA simulations, the half-bridge inverter has been simulated in LTspice in order to obtain waveforms and electrical parameters.

The simulated circuit is that of Fig. 17 with small modifications. The IGBTs are represented by ideal switches in the simulations. The inductive coupling is simulated with the built-in coupled inductor feature, using the component "ind2." The effect of the real part of the mutual impedance is implemented as an arbitrary behavioral voltage source "bv," where the voltage induced by i in j, $V_{r,ij}$, is generated by the mutual resistance R_{ij} and the current of the opposite inductor I_i, $V_{r,ij} = R_{ij}I_i$. The polarity of these elements had to be chosen carefully to produce valid results. A MATLAB script was used to change impedance values for each frequency, run all simulations, and store results.

Fourier transformations were used to calculate the experimental impedance values from inductor voltage, V_{li}, and current, I_i, waveforms

$$Z_{\text{eq}} = V_{l1}/I_1 \tag{22}$$

$$Z_{33} = V_{l3}/I_3. \tag{23}$$

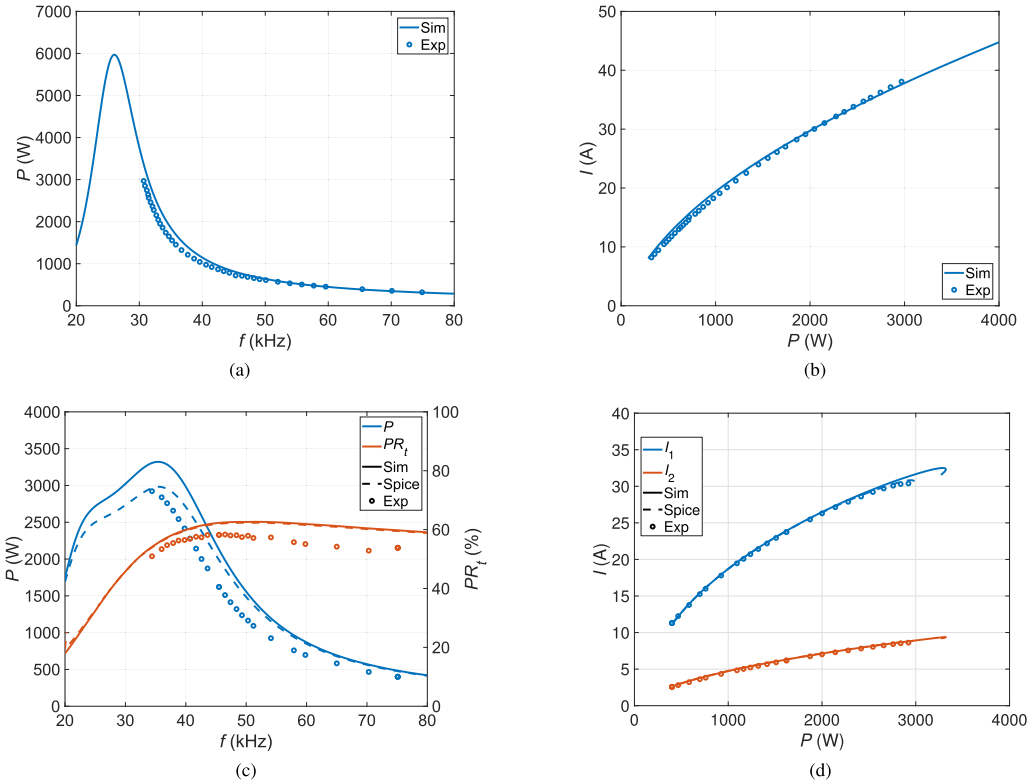

Fig. 22. Power measurements with a disconnected receiver: (a) P and (b) I. Measurements with connected receiver: (c) P and $\mathrm{PR}_{\mathrm{top}}$ and (d) I_1 and I_3.

Z_{11} and Z_{12} can be obtained from measurements with the receiver in an open circuit, if $I_2 = 0$

$$Z_{\mathrm{ind},11} = V_{l1}/I_1 \tag{24}$$

$$Z_{12} = V_{l2}/I_1. \tag{25}$$

Knowing all other terms, Z_{22} can be extracted from (10) as

$$Z_{22} = \frac{Z_{12}^2}{Z_{11} - Z_{\mathrm{eq}}} - Z_{33}. \tag{26}$$

The results are shown in Fig. 20, where the measured values are predicted for the most part by the FEA simulations.

Fig. 21 represents the simulated and measured inductor voltages. Fig. 22 represents the comparison between the simulated and measured values of power, power ratio, and currents when the receiver side is either disconnected [see Fig. 22(a) and (b)] or connected [see Fig. 22(c) and (d)]. Fig. 22(a) shows that the P peak at $\omega_{0,\mathrm{eq}}$ is much higher than the desired P_{max}, 3000 W. Consequently, the equivalent impedance is more inductive at 3000 W and more I is required to deliver the same amount of power than the full system, as shown by comparing Fig. 22(b) and (d). Therefore, reduction of time average PR_t can be achieved by disconnecting the receiver, bearing in mind that high power could be too stressful to the electronics. In Fig. 22(c), the small error in L_{eq} causes a shift of $\omega_{0,\mathrm{eq}}$ and a slight reduction of $\mathrm{PR}_{\mathrm{top}}$, but otherwise simulations were able to predict the experimental results, confirming the validity of the calculation and design method.

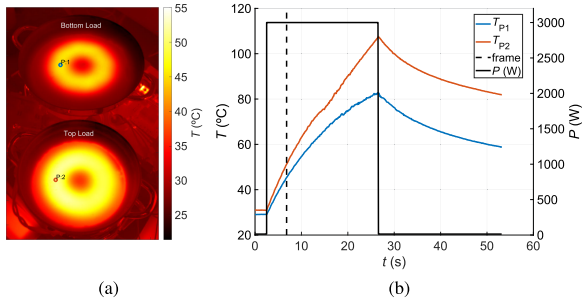

Fig. 23. Thermographic camera measurements with 3000 W. (a) Frame at 6.8 s. (b) Temperature evolution of indicated points.

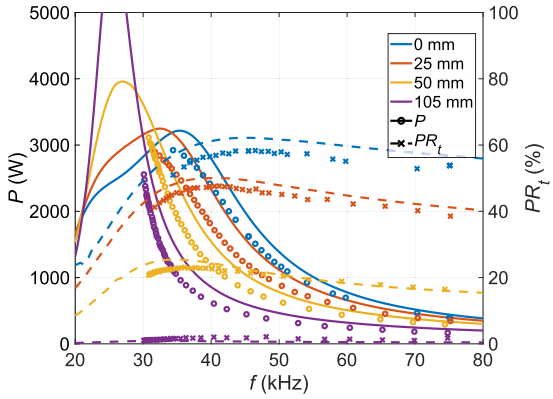

Fig. 24. Measured P and PR_t variation with radial load misalignment.

As a result of a PR_t higher than 50%, more than half of the total power goes to the top load, which is qualitatively shown in Fig. 16 with the bubble density of the boiling water. For further confirmation, Fig. 23 shows the temperature distribution with a thermographic camera when 3000 W is applied to the system with empty vessels until 100 °C is reached.

Fig. 24 shows experimental measurements of P and PR_t with radial misalignment. The measurements confirm the validity of the simulations.

V. Conclusion

The simulations and analytical calculations presented in this article show that IH and inductive coupling can be used in conjunction to deliver power to multiple ferromagnetic loads with a single source in an uncommon IH application. A single cooktop inductor can be used to heat two loads in different planes with an adequate power ratio. This allows heating uncoupled elements that are not directly placed on the top of the cooktop or extending the heating zone for long vessels, such as rectangular grills.

The experimental verification affirms the accuracy of the simulated impedance matrix. In order to maintain a consistent power ratio, global system resonant frequency must be higher than the receiver-side resonant frequency. The ratio between turns of the second and third inductors can be used to modify the power ratio, although their absolute value does not affect equivalent impedance. This degree of freedom can be used to select the relative voltage and current in the receiver side. Full power delivery measurements clearly verify the simulations, with only a small shift in the resonant frequency and a small reduction in the calculated power ratio.

Considering that the power ratio between both loads is currently fixed by geometry and design, further steps should be taken to be able to control the amount of power delivered to each load. For example, a switch in the receiver side could be used to change between operating in a conventional IH configuration with the primary inductor only and the full ICH configuration. The addition of independent power control could also lead to food temperature control inside the oven with additional sensors and electronics.

System misalignment reduces power delivery to the top load, but the system can still operate safely and efficiently. Therefore, the misalignment can be detected and communicated to the user, so that they may correct it. Future work could investigate the compatibility of this kind of system with total active surface cooktops to completely mitigate the misalignment problem.

References

[1] E. Plumed, I. Lope, J. Acero, and J. M. Burdío, "Design of a three inductor system with one externally fed for an inductively coupled heating application," in *Proc. 45th Annu. Conf. IEEE Ind. Electron. Soc.*, Oct. 2019, vol. 1, pp. 5070–5074.

[2] J. Acero *et al.*, "Domestic induction appliances," *IEEE Ind. Appl. Mag.*, vol. 16, no. 2, pp. 39–47, Mar./Apr. 2010.

[3] T. Mishima, C. Takami, and M. Nakaoka, "A new current phasor-controlled ZVS twin half-bridge high-frequency resonant inverter for induction heating," *IEEE Trans. Ind. Electron.*, vol. 61, no. 5, pp. 2531–2545, May 2014.

[4] M. Souley, J. Egalon, S. Caux, O. Pateau, Y. Lefèvre, and P. Maussion, "Optimization of the settings of multiphase induction heating system," *IEEE Trans. Ind. Appl.*, vol. 49, no. 6, pp. 2444–2450, Nov./Dec. 2013.

[5] P. Vishnuram, G. Ramachandiran, S. Ramasamy, and S. Dayalan, "A comprehensive overview of power converter topologies for induction heating applications," *Int. Trans. Elect. Energy Syst.*, vol. 30, no. 10, Aug. 2020, Art. no. e12554.

[6] V. Esteve *et al.*, "Enhanced pulse-density-modulated power control for high-frequency induction heating inverters," *IEEE Trans. Ind. Electron.*, vol. 62, no. 11, pp. 6905–6914, Nov. 2015.

[7] L. Meng, K. W. E. Cheng, and K. W. Chan, "Systematic approach to high-power and energy-efficient industrial induction cooker system: Circuit design, control strategy, and prototype evaluation," *IEEE Trans. Power Electron.*, vol. 26, no. 12, pp. 3754–3765, Dec. 2011.

[8] I. Lope, J. Acero, and C. Carretero, "Analysis and optimization of the efficiency of induction heating applications with litz-wire planar and solenoidal coils," *IEEE Trans. Power Electron.*, vol. 31, no. 7, pp. 5089–5101, Jul. 2016.

[9] E. Plumed, J. Acero, I. Lope, and J. M. Burdío, "Design methodology of high performance domestic induction heating systems under worktop," *IET Power Electron.*, vol. 13, pp. 300–306, Feb. 2020.

[10] J. Villa, J. I. Artigas, J. R. Beltrán, A. D. Vicente, and L. A. Barragán, "Analysis of the acoustic noise spectrum of domestic induction heating systems controlled by phase-accumulator modulators," *IEEE Trans. Ind. Electron.*, vol. 66, no. 8, pp. 5929–5938, Aug. 2019.

[11] O. Lucía, P. Maussion, E. J. Dede, and J. M. Burdío, "Induction heating technology and its applications: Past developments, current technology, and future challenges," *IEEE Trans. Ind. Electron.*, vol. 61, no. 5, pp. 2509–2520, May 2014.

[12] H.-P. Park and J.-H. Jung, "Load-adaptive modulation of a series-resonant inverter for all-metal induction heating applications," *IEEE Trans. Ind. Electron.*, vol. 65, no. 9, pp. 6983–6993, Sep. 2018.

[13] C. Carretero, O. Lucía, J. Acero, and J. M. Burdío, "FEA tool based model of partly coupled coils used in domestic induction cookers," in *Proc. 37th Annu. Conf. IEEE Ind. Electron. Soc.*, Nov. 2011, pp. 2533–2538.

[14] J. Acero, C. Carretero, I. Millán, O. Lucía, R. Alonso, and J. M. Burdío, "Analysis and modeling of planar concentric windings forming adaptable-diameter burners for induction heating appliances," *IEEE Trans. Power Electron.*, vol. 26, no. 5, pp. 1546–1558, May 2011.

[15] C. Carretero, O. Lucia, J. Acero, and J. M. Burdio, "Computational modeling of two partly coupled coils supplied by a double half-bridge resonant inverter for induction heating appliances," *IEEE Trans. Ind. Electron.*, vol. 60, no. 8, pp. 3092–3105, Aug. 2013.

[16] H. N. Pham, H. Fujita, K. Ozaki, and N. Uchida, "Estimating method of heat distribution using 3-D resistance matrix for zone-control induction heating systems," *IEEE Trans. Power Electron.*, vol. 27, no. 7, pp. 3374–3382, Jul. 2012.

[17] J. Serrano, I. Lope, and J. Acero, "Nonplanar overlapped inductors applied to domestic induction heating appliances," *IEEE Trans. Ind. Electron.*, vol. 66, no. 9, pp. 6916–6924, Sep. 2019.

[18] A. Dominguez, L. A. Barragan, J. I. Artigas, A. Otin, I. Urriza, and D. Navarro, "Reduced-order models of series resonant inverters in induction heating applications," *IEEE Trans. Power Electron.*, vol. 32, no. 3, pp. 2300–2311, Mar. 2017.

[19] H. Sarnago, P. Guillén, J. M. Burdío, and O. Lucia, "Multiple-output ZVS resonant inverter architecture for flexible induction heating appliances," *IEEE Access*, vol. 7, pp. 157046–157056, 2019.

[20] J. Davies and P. Simpson, *Induction Heating Handbook*. New York, NY, USA: McGraw-Hill, Oct. 1979.

[21] M. K. Kazimierczuk, *High-Frequency Magnetic Components*. Hoboken, NJ, USA: Wiley, Oct. 2009.

[22] G. A. Covic and J. T. Boys, "Inductive power transfer," *Proc. IEEE*, vol. 101, no. 6, pp. 1276–1289, Jun. 2013.

[23] J. Garnica, R. A. Chinga, and J. Lin, "Wireless power transmission: From far field to near field," *Proc. IEEE*, vol. 101, no. 6, pp. 1321–1331, Jun. 2013.

[24] J. Huang, Y. Zhou, Z. Ning, and H. Gharavi, "Wireless power transfer and energy harvesting: Current status and future prospects," *IEEE Wireless Commun.*, vol. 26, no. 4, pp. 163–169, Aug. 2019.

[25] T. Kan, T.-D. Nguyen, J. C. White, R. K. Malhan, and C. C. Mi, "A new integration method for an electric vehicle wireless charging system using LCC compensation topology: Analysis and design," *IEEE Trans. Power Electron.*, vol. 32, no. 2, pp. 1638–1650, Feb. 2017.

[26] N. Khan, H. Matsumoto, and O. Trescases, "Wireless electric vehicle charger with electromagnetic coil-based position correction using impedance and resonant frequency detection," *IEEE Trans. Power Electron.*, vol. 35, no. 8, pp. 7873–7883, Aug. 2020.

[27] Y. Jiang, L. Wang, J. Fang, C. Zhao, K. Wang, and Y. Wang, "A joint control with variable ZVS angles for dynamic efficiency optimization in wireless power transfer system," *IEEE Trans. Power Electron.*, vol. 35, no. 10, pp. 11064–11081, Oct. 2020.
[28] F. J. López-Alcolea, J. V. D. Real, P. Roncero-Sánchez, and A. P. Torres, "Modeling of a magnetic coupler based on single- and double-layered rectangular planar coils with in-plane misalignment for wireless power transfer," *IEEE Trans. Power Electron.*, vol. 35, no. 5, pp. 5102–5121, May 2020.
[29] W. Han, K. T. Chau, C. Jiang, and W. Liu, "All-metal domestic induction heating using single-frequency double-layer coils," *IEEE Trans. Magn.*, vol. 54, no. 11, Nov. 2018, Art. no. 8400705.
[30] E. Plumed, I. Lope, J. Acero, and J. M. Burdio, "Inductor system evaluation for simultaneous wireless energy transfer and induction heating," in *Proc. 44th Annu. Conf. IEEE Ind. Electron. Soc.*, Oct. 2018, pp. 3509–3514.
[31] R. C. M. Gomes, M. A. Vitorino, D. A. Acevedo-Bueno, and M. B. de Rossiter Corrêa, "Multiphase resonant inverter with coupled coils for AC-AC induction heating application," *IEEE Trans. Ind. Appl.*, vol. 56, no. 1, pp. 551–560, Jan./Feb. 2020.
[32] W. Han, K. T. Chau, and Z. Zhang, "Flexible induction heating using magnetic resonant coupling," *IEEE Trans. Ind. Electron.*, vol. 64, no. 3, pp. 1982–1992, Mar. 2017.
[33] W. Han, K. T. Chau, Z. Zhang, and C. Jiang, "Single-source multiple-coil homogeneous induction heating," *IEEE Trans. Magn.*, vol. 53, no. 11, Nov. 2017, Art. no. 7207706.
[34] E. Plumed, I. Lope, and J. Acero, "Induction heating adaptation of a different-sized load with matching secondary inductor to achieve uniform heating and enhance vertical displacement," *IEEE Trans. Power Electron.*, vol. 36, no. 6, pp. 6929–6942, Jun. 2021.
[35] M. Kim, H. Park, and J. Jung, "Practical design methodology of IH and IPT dual-functional apparatus," *IEEE Trans. Power Electron.*, vol. 35, no. 9, pp. 8897–8901, Sep. 2020.
[36] J. Sakellaris, G. Meunier, A. Raizer, and A. Darcherif, "The impedance boundary condition applied to the finite element method using the magnetic vector potential as state variable: A rigorous solution for high frequency axisymmetric problems," *IEEE Trans. Magn.*, vol. 28, no. 2, pp. 1643–1646, Mar. 1992.

Emilio Plumed (Member, IEEE) received the M.Sc. degree in industrial engineering in 2016 from Universidad de Zaragoza, Zaragoza, Spain, where he is currently working toward the Ph.D. degree in electronic engineering with the Department of Electronic Engineering and Communications.

His research interests include electromagnetic modeling of induction heating (IH) systems and hybrid IH and wireless power transfer systems.

Ignacio Lope (Member, IEEE) received the M.Sc. degree in electrical engineering and the Ph.D. degree in power electronics from Universidad de Zaragoza, Zaragoza, Spain, in 2010 and 2015, respectively.

He is currently with BSH Home Appliances, Zaragoza, where he is involved in several projects focusing on developing domestic induction heating appliances. He is also an Adjunct Professor with the Department of Applied Physics, Universidad de Zaragoza. His current research interests include electromagnetic modeling of inductive coupled contactless energy transfer systems and loss modeling of magnetic devices.

Jesús Acero (Senior Member, IEEE) received the M.Sc. and Ph.D. degrees in electrical engineering from Universidad de Zaragoza, Zaragoza, Spain, in 1992 and 2005, respectively.

From 1992 to 2000, he worked in several industry projects, especially focused on custom power supplies for Research Laboratories. Since 2000, he has been with the Department of Electronic Engineering and Communications, Universidad de Zaragoza, where he is currently a Professor. His main research interests include resonant converters for induction heating applications, inductive-type load modeling, and electromagnetic modeling.

Dr. Acero is a member of the IEEE Power Electronics Society, the IEEE Industrial Electronics Society, the IEEE Magnetics Society, and the Instituto de Investigación en Ingeniería de Aragón.

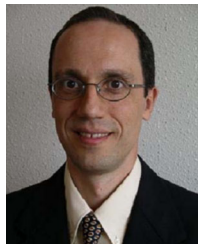

José Miguel Burdío (Senior Member, IEEE) received the M.Sc. and Ph.D. degrees in electrical engineering from the University of Zaragoza, Zaragoza, Spain, in 1991 and 1995, respectively.

He is currently a Professor with the Department of Electronic Engineering and Communications, University of Zaragoza, where he is the Head of the Group of Power Electronics and Microelectronics and the Director of the BSH Power Electronics Laboratory. In 2000, he was a Visiting Professor with the Center for Power Electronics Systems, Virginia Tech, Blacksburg, VA, USA. He has authored or coauthored more than 100 international journal papers and 250 papers in conference proceedings. He is a co-inventor of more than 60 patents. His main research interests include modeling of switching converters and resonant power conversion for induction heating and biomedical applications.

Dr. Burdío is a senior member of the IEEE Power Electronics Society, the IEEE Industrial Electronics Society, and the IEEE Engineering in Medicine and Biology Society and a member of the Instituto de Investigación en Ingeniería de Aragón.